Saturn's F Ring: Kinematics and Particle Sizes from Stellar Occultation Studies[1]

A. S. Bosh[2] and C. B. Olkin

Lowell Observatory, Flagstaff, Arizona 86001-4499
E-mail: amanda@lowell.edu

R. G. French

Department of Astronomy, Wellesley College, Wellesley, Massachusetts 02481

and

P. D. Nicholson

Department of Astronomy, Cornell University, Ithaca, New York 14853-6801

The occultation of GSC5249-01240 by Saturn's rings was observed in a spectrally resolved mode using the Faint Object Spectrograph on the Hubble Space Telescope. By combining these data with other occultation data, we have determined the inclination of the F ring to be 0.0065 ± 0.0014 deg. Our inclined F ring orbit model explains an abrupt decrease in flux at the west ansa of the ring that was observed during the November 1995 ring-plane crossing as well as the nondetection of 1995 S5 during one set of observations in November 1995. The F ring's equivalent depth is found to have no significant dependence on wavelength between 0.27 and 0.74 μm, indicating the presence of a population of ring particles larger in size than $\sim$10 μm. This contrasts with the results from a previous analysis of Voyager images at various phase angles, in which the particles were determined to be predominantly submicron in size. The difference may be due to temporal or longitudinal variability within the ring. © 2002 Elsevier Science (USA)

Key Words: planetary rings, Saturn; occultations; orbits.

1. INTRODUCTION

During the Voyager flybys the F ring was revealed as a dynamically intriguing ring, with its multiple strands and shepherd satellites. During the most recent ring-plane crossing in 1995–1996, several bodies that are assumed to be clumps within the

F ring were discovered by various observers (Bosh and Rivkin 1996, Nicholson *et al.* 1996, Roddier *et al.* 2000, McGhee *et al.* 2001). Thus, an accurate kinematic model for the F ring is important for goals such as determining the dynamical relationships between the ring and nearby satellites, and whether the objects seen during the 1995 ring-plane crossing reside within this ring. Through analysis of 13 stellar occultation data sets from 1980–1995, we determine the kinematics of the F ring. One event in 1995 that was observed near the solar ring-plane crossing is unusually sensitive to ring inclinations; using these data we establish a nonzero inclination for the F ring. This occultation was observed in a spectrally resolved mode, providing information on the wavelength dependence of the ring's equivalent depth. From this we are able to place constraints on particle properties within the ring.

2. DATA AND GEOMETRIC ANALYSIS

Every $\sim$15 years Saturn's ring plane sweeps across the Earth and Sun; during such events, the rings appear very dark when viewed from Earth. These infrequent periods of low reflected light from the rings are valuable opportunities for studying the small inner satellites and the rings themselves. The most recent ring-plane crossing season was 1995–1996; the nearly edge-on view of the rings at this time aids in detection of any out-of-plane component of the rings, i.e., inclinations. Serendipitously, Saturn's rings occulted the star GSC5249-01240 (Bosh and McDonald 1992) during the period when the plane of the rings crossed the Sun's disk (Fig. 1). The stellar occultation technique—monitoring stellar flux as the star passes behind a solar system body—yields data with potentially high spatial resolution (approximately 1 km at Saturn at visible wavelengths)
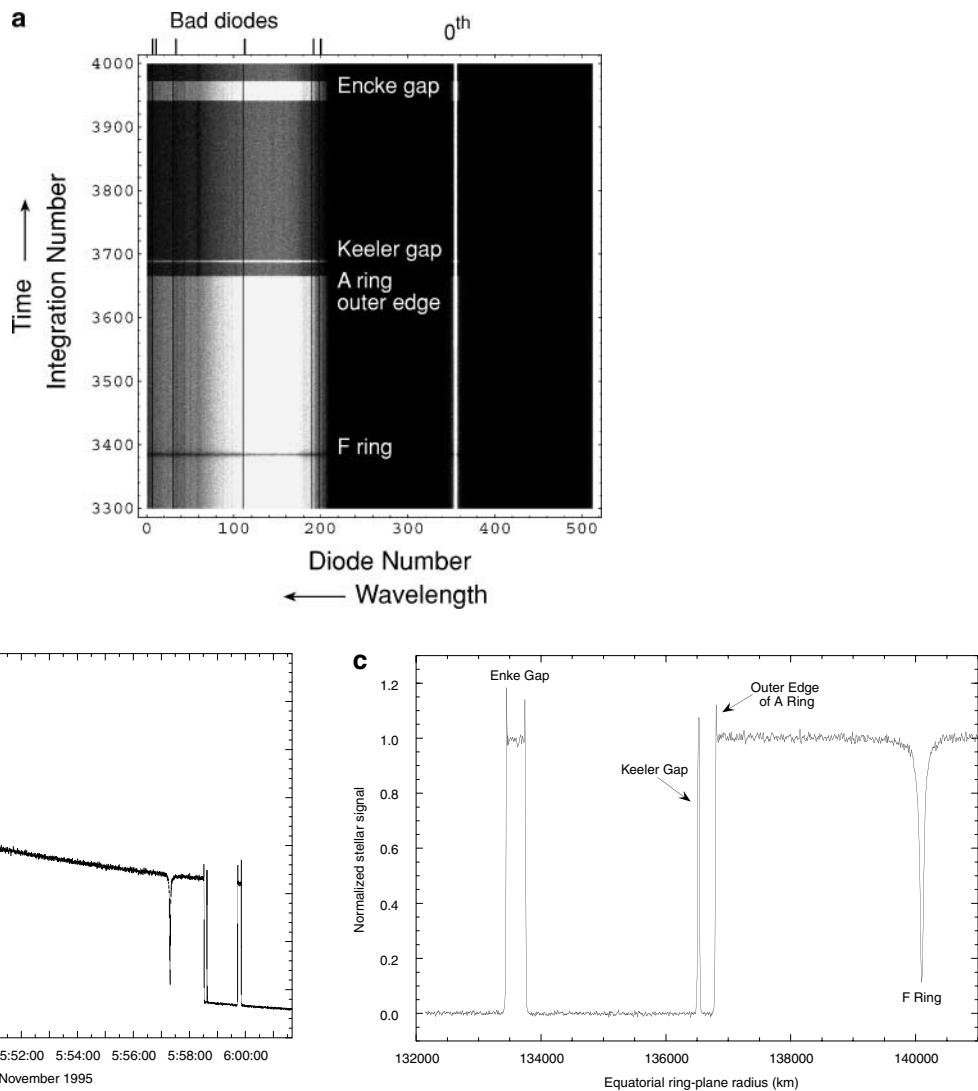

FIG. 1. The occultation of GSC5249-01240 by Saturn's rings, as observed with the HST's Faint Object Spectrograph (FOS). (a) A portion of the FOS F ring data segment. The grayscale indicates signal level; white is brighter. The occulted star is the source, therefore when it is bright the rings are optically thin, and when it is dark the rings are optically thick. This segment includes (from bottom) the F ring (dark horizontal line), the outer edge of the A ring (transition from bright to dark), the Keeler gap (bright horizontal line), and the Encke gap (bright horizontal band). (b) Binned signal (all 512 diodes) from the entire F ring data segment. The brighter signal at the beginning of this segment arises because the aperture starts closer to Saturn, then slowly moves away. Contributions to the background include scattered Saturn-shine, and reflected and transmitted ring light. (c) The geometric solution for the F ring segment. Stellar signal is normalized to its unocculted value. All observed times are converted to equatorial ring-plane radii using the geometric solution described in Section 2. Note that because the F ring does not lie in the equatorial plane, its radius in this figure is the ring's projection onto the equatorial plane rather than its actual distance from Saturn. The instances when the stellar signal rises above its unocculted value (Encke gap, Keeler gap, outer edge of the A ring) is a result of the diffraction profile at a sharp edge. Previously seen in other occultation events, they verify the sharp transitions at these feature boundaries. In contrast, the F ring's lack of a similar diffraction profile indicates a more gradual transition, in either the radial or vertical direction, or in both directions.

and therefore allows us to improve ring kinematic models (e.g., Elliot *et al.* 1993, French *et al.* 1993, Hubbard *et al.* 1993, Bosh 1994).

Occultation of GSC5249-01240

The occultation of the star GSC5249-01240 (B = 12.2; Bosh and McDonald 1992) was observed with the Hubble Space Telescope (HST) using the Faint Object Spectrograph (FOS; Keyes

1995), and from the Infrared Telescope Facility (IRTF) using NSFCAM (Shure *et al.* 1994). The FOS in "RAPID" mode produces time-resolved spectra of the sources in a 0.86-arcsec circular aperture (FOS designation "1.0"); in this case, the sources were the occulted star, the ring background, and scattered light from Saturn. The ring signal was much lower than usual because this event occurred when the Sun and Earth were on opposite sides of the ring plane; the residual ring flux was due to diffusely transmitted rather than reflected sunlight. This greatly

increased the signal-to-noise ratio (S/N) of the data. We used the G650L grating with the red digicon, obtaining wavelength coverage from 2700 to 7400 Å with a dispersion of -25.44 Å diode^{-1}. The primary spectrum covered diodes 67 to 211 out of 512 total diodes. The zeroth-order spectrum was also recorded at diode number ~355 and was utilized when all of the signal was binned together (Fig. 1). The RAPID mode is not a standard supported mode for FOS, so flux calibration via the standard data pipeline was not performed. The combined star plus ring signal (with a small amount of scattered light from Saturn) varied as the optical depth τ of the ring affected the stellar signal and as position in the rings affected the amount of background signal. The ring occultation data were obtained in four sections, each corresponding to one-half of one HST orbit around the Earth. For the F ring segment, the data collection period was 1230 s long. For each integration, the exposure time was 0.25 s with an overhead (for reading diodes) of 0.037 s, resulting in a cycle time of 0.287 s. All RAPID parameters were set to minimize over-

head time and thus maximize the observing efficiency (exposure time divided by cycle time).

The IRTF data for this same event were obtained with NSFCAM in "movieburst" mode, using the Spencer 2.3-μm filter to reduce scattered light from Saturn. Subframes of 160×56 0.3-arcsec pixels were obtained that included Saturn, the faint rings, the occulted star, a comparison star, and a satellite. We did not correct the images for flat-field effects because the star remained in the same portion of the chip for the ring event and because this was a relatively small correction. For photometry we found that the rings were faint enough that ring background subtraction was not necessary; a 10×10 pixel extraction box was used for the occulted star, whereas a 7×7 pixel box was used for the comparison star. For the F ring segment, the integration time was 1.0 s with a deadtime of 0.043 s for a cycle time of 1.043 s. The apparent ring-plane radial velocity of the star at the time of the F ring event was approximately 12 km sec^{-1}, thus the radial resolution of these data was approximately 12 km. This rather

TABLE I
Geometric Model Parameters

Saturn ring-plane pole	
Reference	Bosh 1994
α (deg, J2000)	40.59287
δ (deg, J2000)	83.53833
Epoch	UTC 1980 November 12 23:46:00
$\partial\alpha/\partial t$ (deg yr^{-1}, J2000)	-0.00061772
$\partial\delta/\partial t$ (deg yr^{-1}, J2000)	-0.00006420

Gravitational harmonic coefficients	
Reference	Nicholson and Porco 1988
J_2	0.016297
J_4	-0.000910
J_6	0.000107
Equatorial radius	60330 km

Stars

Event and date	Star position (J2000) α	δ	Station	Time offset (t_0, sec)	Ephemeris identifier for: Planets	Satellites
GSC5249-01240 21 November 1995	23 19 34.5985	-6 47 10.4737	HST	0.0	DE406	SAT077
			IRTF	0.0	DE406	SAT077
GSC6323-01396 3 October 1991	20 10 30.3637	-20 36 47.7081	HST	0.0	DE130	SAT031
28 Sgr 3 July 1989	18 46 20.5849	-22 23 32.1783	ESO 1-m	0.166	DE130	SAT018H
			ESO 2-m	0.146	DE130	SAT018H
			IRTF	0.0	DE130	SAT018H
			McDonald	-0.077	DE130	SAT018H
			Palomar	-0.033	DE130	SAT018H
δ Sco 26 August 1981	16 00 20.0182	-22 37 17.642	PPS	0.094	DE130	t811001
Voyager 1 RSS 13 November 1980			DSS-63	-0.011	DE130	t810308

long cycle time and resulting coarse spatial resolution were cho-
sen to optimize the amount of data obtained over the entire ring
event. Because all images for a run are stored in memory, the
NSFCAM run time is limited by total memory available; thus,
there is a trade-off among total coverage, integration time, and
subframe size.

Geometric Analysis

To convert observed times to ring-plane radii, we combine
these data with other Saturn ring occultation data. As described
in Bosh (1994) and Elliot *et al*. (1993), we use solar system
barycentric ephemerides for the Earth, the Saturn barycenter,
and the Voyager spacecraft; system barycentric ephemerides for
Saturn's major satellites; and geocentric ephemerides for the
Hubble Space Telescope. We use astrometric star positions in a
vector-based analysis to convert the observed times of specific
events to distance from the center of Saturn. Parameters used
in this geometric model are listed in Table I. We incorporate
data from five occultations, with a total of 13 F ring points to
determine the F ring orbit (Table II). F ring radial profiles for
some of these data sets are plotted in Fig. 2. The RMS residual
per degree of freedom for circular ring features in the 1995
data is 8.7 km for HST and 14.0 km for IRTF. Although larger
than usual for stellar occultation data (other Saturn ring data
sets are $\sim$1–2 km), we expect residuals of this magnitude given
the sampling frequency and the extreme foreshortening of the

ring plane. The geocentric sky-plane velocity for this event is
only 0.9 km sec^{-1} because Saturn was near its stationary point.
Radial velocity in the ring plane is much larger because the rings
were nearly edge-on. When combined with observer velocity
and integration time, the sampling bin size in the ring plane is
approximately 14 km for the IRTF observations, and varies from
$\sim$0 to 14 km for the HST observations.

3. KINEMATIC MODEL

During an occultation observation, as the ring sweeps across
the star it attenuates the stellar signal and the time of this sig-
nal drop is noted by the observer. Ephemerides for planet, ob-
server, and source (if necessary) are then incorporated to cal-
culate where and when the drop occurred at the planet for an
assumed ring plane. Different observed times are therefore usu-
ally interpreted as different radii and longitudes in an equatorial
ring; however, a ring's inclination will affect its observed time,
most dramatically when the rings are near to edge-on. For a ring
with small inclination, at moderate values of ring opening angle
B, the change in observed time is small and therefore is easily
absorbed into the scatter about a coplanar fit. For B near 0$°$,
however, the change in apparent radius can be large (>100 km
for the 1995 event, at B of 2.67$°$) and thus places a strong
constraint on the ring's inclination and node. The longitude
probed by the occultation also affects the sensitivity: the further
from either node the occultation probes, the more sensitive to

TABLE II
Occultation Data Used in Fitting F Ring Orbit Parameters

Event	Observing station	Observed time (UTC; y m d h:m:s)	Obs. radius in ring plane^a(km)	Corotating longitude^b (deg)	True anomaly (deg)	Longitude from node (deg)	B (deg)	S^c (km)	Residual^d (km)	RMS^e (km)	Reference^f
GSC5249–01240	HST	1995 11 21 05:57:18.755	139945.89	64.8	320.2	154.7	2.7	132.0	−4.7	8.7	this work, O96
GSC5249–01240	IRTF	1995 11 21 07:58:49.227	139940.70	19.9	324.3	159.2	2.7	105.0	5.4	14.0	this work, O96
GSC6323–01396	HST	1991 10 03 13:31:37.995	140079.28	236.4	66.0	46.6	21.4	13.8	0.1	1.8	E93
28 Sgr	ESO-1m	1989 07 03 06:01:39.01	140185.79	142.6	276.3	146.5	25.4	−11.2	0.8	1.3	F93
28 Sgr	ESO-1m	1989 07 03 09:28:57.36	140375.05	259.5	116.5	347.5	25.4	−2.0	−7.4	1.3	F93
28 Sgr	ESO-2m	1989 07 03 06:01:38.97	140186.27	142.6	276.3	146.5	25.4	−11.2	1.3	1.6	F93
28 Sgr	IRTF	1989 07 03 09:31:01.947	140325.27	252.4	110.3	341.3	25.4	−4.1	−21.9	1.0	Ha93, F93
28 Sgr	McDonald	1989 07 03 05:58:47.922	140149.07	149.2	281.7	151.9	25.4	−8.3	−2.6	0.8	F93
28 Sgr	McDonald	1989 07 03 09:27:10.867	140352.54	254.0	110.4	341.3	25.4	−4.1	5.1	0.8	F93
28 Sgr	Palomar	1989 07 03 05:59:34.77	140149.85	149.0	281.8	152.0	25.4	−8.2	−1.2	1.0	F93
28 Sgr	Palomar	1989 07 03 09:27:47.44	140345.22	253.3	109.9	340.9	25.4	−4.3	0.5	1.0	F93
δ Sco	Voyager2 PPS	1981 08 26 01:51:00.01	140377.23	11.5	115.4	12.5	28.7^g	2.4	1.0	1.2	L82, N90
Voyager1 RSS	DSS-63	1980 11 13 04:59:13.01	140513.39	105.7	215.9	12.8	5.9	28.8	1.6	1.2	T81, N90

^{a} Distance from the center of Saturn at the observed longitude, in the inclined ring plane.

^{b} Longitude at 2000 January 1 12:0 UT, corotating at the mean motion of the F ring, using the adopted solution in Table III.

^{c} Sensitivity S of data point to inclination is defined as: $i * \partial r/\partial i$.

^{d} Radial residuals (observed—model) for the adopted solution (Fit #3) in Table III.

^{e} RMS for circular features only using Bosh (1994) ring pole solution (Table I).

^{f} References are Elliot *et al*. (1993, E93), French *et al*. (1993, F93), Harrington *et al*. (1993, Ha93), Lane *et al*. (1982, L82), Nicholson *et al*. (1990, N90), Olkin
and Bosh (1996, O96), and Tyler *et al*. (1981, T81).

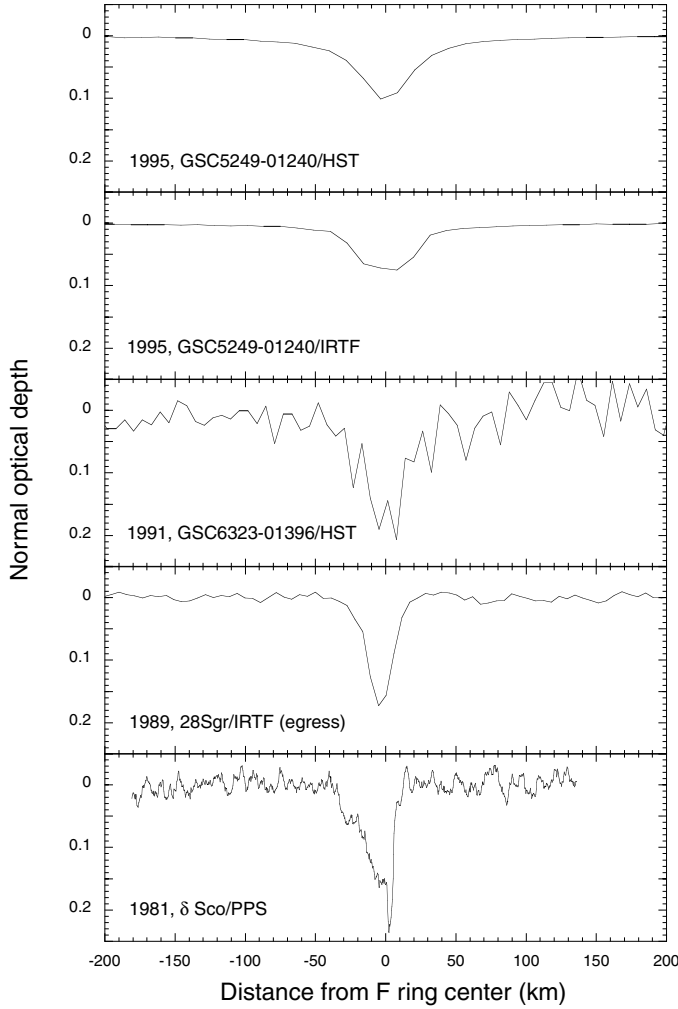^{g} As viewed from Voyager 2 at Saturn (Esposito *et al*. 1987).

FIG. 2. F ring radial profiles from five occultation data sets, 1981–1995. The normal optical depth of the F ring is seen to be variable. This is an example of the longitudinal variability found in this ring. Radial structure is not directly comparable across data sets because radial resolution differs. The profile for the 1991 occultation of GSC6323-01396 is scaled to the approximate level of the other data in this figure; actual levels are not known as the flux calibration for these data is uncertain due to varying amounts of star and background signal included in the aperture.

inclination the measurement will be. The sensitivity of each data set ($S = i\,\partial r/\partial i$; Table II) is the difference in apparent radius between an inclined and non-inclined (coplanar) feature, taking into account the angle from the node.

Using the method described in Bosh (1994), we perform an unweighted fit of an inclined Keplerian ellipse model to the observed occultation times of Saturn's F ring from the data sets described in Table II. The model is specified by the parameters semimajor axis a, eccentricity e, longitude of pericenter ϖ_0, pericenter precession rate $\dot{\varpi}$, inclination i, longitude of ascending node Ω_0, node regression rate $\dot{\Omega}$, and reference epoch t_0. Longitudes are measured with respect to the Earth's mean equator and dynamical equinox at J2000.

In Table III we present our suite of least-squares fits to the occultation data. Fit #1 describes an inclined model in which the precession/regression rates are not fit but instead are calculated from the zonal gravity harmonics J_{2n}. Two points have high residuals in this fit—the 28 Sgr/IRTF observation and the δ Sco/PPS observation. (We refer to the occultation data in Table II as *star/observing station*, except for GSC stars that are labeled *year/observing station*.) The δ Sco/PPS datum places a strong constraint on the precession rate because its true anomaly is similar to 28 Sgr egress true anomalies and because the time baseline is almost eight years. We modify our fitting procedure to allow the precession rate to be a free parameter to account for the contribution due to perturbations from nearby satellites and rings (Nicholson and Porco 1988). The nodal regression rate is similarly affected and should be a free parameter as well, but in practice there are too few data points to constrain this quantity—only two data points from the same epoch (1995) are highly sensitive to the node location. Instead we "link" the regression rate to the precession rate by realizing that the "extra" precession—the ring and satellite contribution, which is the difference between the fitted parameter and the value calculated from the J_{2n}—is approximately equal and of opposite sign for the regression rate. Fit #2 encompasses these changes and the δ Sco/PPS residual is dramatically reduced. The 28 Sgr/IRTF point still has a large residual. For our adopted solution (Fit #3, Fig. 3), we remove the 28 Sgr/IRTF point (possible causes for its large residual are discussed below). To test the sensitivity of the solution to our chosen value for Saturn's pole position, we refit the model using the French *et al.* (1993) pole position (Fit #4) and find no significant change in the orbit parameters.

The 1995/HST and 1995/IRTF data are the main constraints on the inclination. However, earlier data are not completely insensitive as may be seen from the values for S in Table II. As previous coplanar fits (R. French, unpublished, as used by Nicholson *et al.* 1996) include only data acquired before 1990, we perform Fits #5 and #6 to test the extent to which the inclination influences these results. First we fit a coplanar solution to the earlier data (Fit #5), then fix the inclination and node at our adopted value and refit for the planar parameters (Fit #6). Our results show a significant difference in a and e (5–6 σ), confirming that the earlier solutions were indeed skewed by those points that are somewhat sensitive to inclination. As mentioned before, changes in event timing due to inclination are interpreted as radius shifts and thus lead to a larger fitted eccentricity with similar RMS residual.

Finally, we compare our result with previous independent orbit fits by Synnott *et al.* (1983) and Murray *et al.* (1997), which were derived using measurements of Voyager images. Longitudes are converted to our system and epoch for comparison. The Synnott *et al.* and Murray *et al.* results for semimajor axis, eccentricity, and longitude of pericenter are consistent with ours, but are not sensitive to inclinations.

A possible cause for concern is the fairly limited coverage of the available data. Data are available from only five epochs,

TABLE III
F Ring Orbit Solutions

Fit #	Description	Semimajor axis, a (km)	Eccentricity, $e \times 10^3$	Long. of pericenter,[a] ϖ (deg)	Precession rate, $\dot\varpi$ (deg day^{-1})	Inclination, i (deg)	Long. of ascending node,[a] Ω (deg)	Regression rate, $\dot\Omega$ (deg day^{-1})	RMS (km)
1	ϖ and $\dot\Omega$ calculated from J_{2n}	140222.1 ± 4.8	2.59 ± 0.13	16.0 ± 1.5	2.6981	0.0046 ± 0.0010	38.9 ± 13.6	-2.6856	13.7
2	ϖ fitted, linked $\dot\Omega$	140221.6 ± 3.0	2.50 ± 0.08	25.5 ± 2.5	2.7003 ± 0.0006	0.0072 ± 0.0011	12.2 ± 4.7	-2.6879	9.2
3[b]	ϖ fitted, linked $\dot\Omega$; w/o 28 Sgr/IRTF pt.	140223.7 ± 2.0	2.54 ± 0.05	24.1 ± 1.6	2.7001 ± 0.0004	0.0065 ± 0.0007	16.1 ± 3.6	-2.6876	5.7
4	French *et al.* (1993) pole	140223.7 ± 2.0	2.53 ± 0.06	24.1 ± 1.6	2.7001 ± 0.0004	0.0064 ± 0.0007	17.3 ± 3.9	-2.6877	5.8
5	Pre-1990 data only, coplanar	140211.6 ± 2.7	2.87 ± 0.06	26.3 ± 1.6	2.7003 ± 0.0003	0.0	—	—	5.5
6	Pre-1990 data only, fix i at adopted soln. value	140222.6 ± 2.1	2.57 ± 0.05	24.7 ± 1.4	2.7002 ± 0.0003	0.0065	16.0	-2.6877	4.3
—	Synnott *et al.* (1983) solution[c]	140185 ± 30	2.60 ± 0.60	20 ± 15	—	0.0 ± 0.1	—	—	—
—	Murray *et al.* (1997) solution,[c] γ strand	140219 ± 4	2.79 ± 0.02	25.3 ± 1.6	—	—	—	—	—

[a] Longitudes are measured in the J2000 system, from the intersection of the planet's equatorial plane with the Earth's. The reference time is the J2000 epoch.

[b] Adopted solution. The adopted uncertainties in inclination and node location are to be increased by a factor of 2 over those in this table to account for the possibility of an undetected eccentricity variation.

[c] The Synnott *et al.* (1983) and Murray *et al.* (1997) values for longitude of periapse have been converted to our system for inclusion in this table, using the precession rate for the adopted solution.

while the kinematic model contains six free parameters. The 1995 data yield one cluster of points and are clearly are required to fit for the inclination parameters (i, Ω); however, they do not provide the only constraint on these parameters—the Voyager 1 RSS data point is less sensitive, but only by a factor of $\sim$4 (as compared to factors of $\sim$50 for some 28 Sgr points). The shape

FIG. 3. Data, model, and residuals for Fit #3 in Table III (adopted solution) plotted against true anomaly. The largest residual, that of 28 Sgr/IRTF is off the bottom of the plot at -22 km, and is indicated by the arrow. The RMS residual of the fit, 5 km, is due largely to the scatter of the two 1995 points (a result of the lower spatial resolution of these data) and the relatively large scatter of the 28 Sgr egress points near true anomaly of $120°$ (possibly due to the proximity of Prometheus increasing local variations in the ring).

parameters (a, e, ϖ_0) are set largely by the dense coverage of the 28 Sgr data: seven data points (excluding IRTF) for ingress and egress from both northern and southern hemisphere stations leads to four clusters of data points. The 1991 observation adds another unique datum. Adding in the two Voyager points we have eight clusters of longitudes at five epochs. From just the pre-1990 it is easy to fit for a, e, and ϖ_0, as evidenced by Fits #5 and #6 in Table III. Fit #5 is close to the adopted solution in a and e, but still about 5σ away. This is due to the facts that none of the data are completely insensitive to inclination and that an inclined ring modeled as a coplanar ring will have a modified a and e because of projection effects. Thus, when we fix the inclination and node at the adopted values (Fit #6), the semimajor axis and eccentricity from just 28 Sgr, and Voyager data are indistinguishable from the adopted solution. This result still holds when Voyager data are excluded and only 28 Sgr data are used.

Without the extreme sensitivity of the 1995 data to inclinations, the fit of an inclined Keplerian ellipse to these data would contain much greater uncertainty due to the propagated effect of an unknown inclination. Given the known vagaries of the F ring and the lack of dense coverage at most epochs, it is possible that additional effects are present but not yet recognized or that this kinematic result is wrongly influenced by an unrecognized spurious datum of the 28 Sgr/IRTF type.
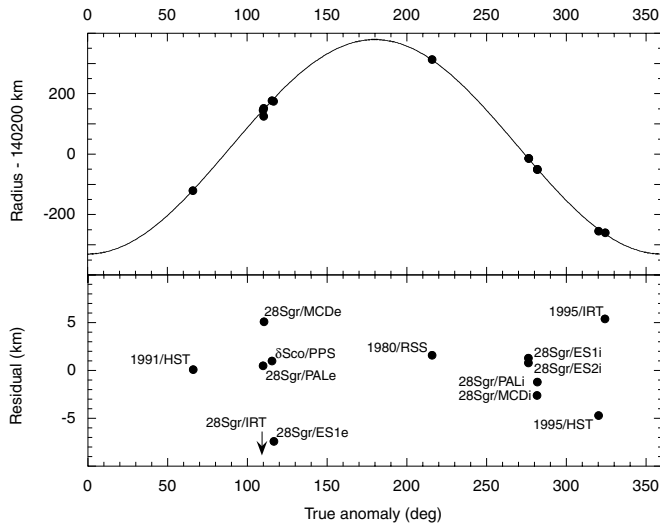
Fit Residuals

The RMS residual of the adopted solution is 5.7 km, consistent with the RMS for circular features for the 1995 data (both HST and IRTF). However, the 28 Sgr/IRTF egress point has a residual of -22 km, or over 1 s in time. We consider two possible causes

of this high residual: problems with the data set or variability in the F ring. Data-set problems include timing errors or station location errors. We eliminate many possible sources of error within the data set by noting that the 28 Sgr/IRTF RMS residual from fits to known circular features is 0.96 km, comparable to the 0.79–1.92 km obtained for other 28 Sgr data sets (Bosh 1994); similar values were obtained by French *et al.* (1993). Thus, an overall timing calibration, station location, or other systematic error specific to this data set is unlikely as it would have affected the many circular features as well. The 28 Sgr/IRTF data suffer from timing glitches that were identified and corrected during the course of the data analysis (Harrington *et al.* 1993); we investigate the possibility that one such glitch was missed. Timing glitches occurred as a result of loss of lock in the phase-locked loop signal that tied the portable quartz oscillator clock to the camera's computer. Each loss of lock was obvious in the timing signal as a few seconds of frequency oscillation, and in each of the 42 cases added 2 or 3 extra interrupts to the time stream. Each added interrupt makes the recorded time seem later than the actual time. Because the timing stream was not reset during the event, the effects of these timing glitches is cumulative over the recording interval. Therefore, a timing problem at any point is necessarily due to all the glitches that occurred before that point. The last known glitch occurred during egress in the inner A ring and was successfully corrected, as circular features in the outer A ring show no unusual residuals. Harrington and Bosh reexamined the timing data and found no previously undetected glitches before the F ring egress observation. In addition, the model for the 28 Sgr/IRTF point is at a larger ring-plane radius than the observation. If this were caused by a timing glitch, the recorded time would have been earlier than the actual time, a shift in the opposite direction of all known timing glitches in this data set.

Corroboration of the 28 Sgr/IRTF data point is provided by data obtained from the same occultation at the nearby United Kingdom Infrared Telescope (UKIRT; Hubbard *et al.* 1993). These two telescopes are separated by less than 0.5 km so their observed feature times should differ by very little, with the exact amount depending on the direction of the shadow path on the ground. For these two data sets, the observed F ring timing differs by less than 0.1 s, or 2.2 km (W. B. Hubbard, private communication). Although the UKIRT point is not included in our fits, it is clear that it too would have a similarly high residual. This suggests that the observed large 28 Sgr/IRTF residual is a real feature in the rings and not an artifact in the data.

When considering intrinsic F ring variability as the cause of the large residual, there are several effects that may contribute. Voyager images reveal a ring that is very different from the uniform elliptical wire often used in modeling narrow rings. In contrast, the real F ring sometimes separates into multiple strands (Murray *et al.* 1997), although these have never been observed in occultation profiles; contains clumps whose range of mean motions translates to a semimajor axis spread of greater than 20 km (Showalter 1997); and is not smoothly elliptical but instead contains local "kinks" of similar amplitudes. Models

of the interactions between Prometheus and the ring show that passages of Prometheus can "throw" segments of the F ring an average of 1–1.5 km and up to 10 km (Showalter, *et al.* 1999). Given this variety of observed or modeled non-Keplerian behavior and the sparse data available, a definitive explanation for the 28 Sgr/IRTF residual is elusive.

While the cause of the 28 Sgr/IRTF residual remains unknown, the inclination solution is largely unaffected by this datum due to its lower sensitivity to out-of-plane displacement (Table II). Removing this point from the fit does not alter the fitted ring-orbit parameters in a significant way, but does reduce the 1σ errors (Table III, Fits #2 and #3).

Secular Interactions with Prometheus

The F ring and Prometheus are predicted to be involved in an intricate dance, with Prometheus colliding with the core of the F ring every ∼19 years (Murray and Giuliatti Winter 1996; hereafter MGW96). The last collision was predicted to have occurred in February 1994 ±1.7 years. Using the latest values for orbital parameters of Prometheus (French *et al.* 1998) and the F ring (Table III), we find that their orbits do not intersect, with a center-to-center close approach distance of 337 km (Prometheus' longest radius is 70 km) for aligned nodes and anti-aligned pericenters. However, this calculation ignores any periodic change in the eccentricity of the F ring due to secular perturbations from its shepherd satellites. Borderies *et al.* (1983) predicted that the F ring's eccentricity will vary with an 18-year period, and is 20% greater at closest approach to Prometheus than when differential precession takes them further away. MGW96 predict a periodic change in eccentricity from 0.00257 to 0.00288 with a period of 19.08 years. Both results are based on initial conditions from Synnott *et al.* (1983), which are different from those presented and used here.

We attempt to establish the maximum effect of a variable eccentricity that is consistent with the data. The parameters in this model are mean eccentricity e_0, eccentricity half-amplitude h_e, period T, reference time t_0, and angular offset θ_0:

$$e(t) = e_0 + h_e \sin\left[\frac{2\pi(t - t_0)}{T} + \theta_0\right]. \quad (1)$$

We fix θ_0 at $\pi/2$, where $e(t)$ is a maximum. The reference time t_0 is then the time of closest approach between Prometheus and the F ring. We cannot fit for all parameters at once because our data are too sparse, so we fix some parameters at the values given by MGW96; the free parameters for variable eccentricity in the least squares fits are e_0 and h_e (Table IV). We begin by fixing the period and reference time at the MGW96 values of 19.08 years and 6 February 1994, and performing an unweighted fit to the data (including 28 Sgr/IRTF); this is Fit #7 in Table IV. This fit returns a statistically marginal eccentricity amplitude h_e. Inspection of the fit residuals shows that this fit is suspect; it achieves the listed results by significantly reducing the residuals

TABLE IV
Variable Eccentricity Solutions

Fit #[a]	Description[b]	Semimajor axis, a (km)	Eccentricity, $e \times 10^3$	Eccentricity ampl., $h_e \times 10^3$	Long. of pericenter,[c] ϖ (deg)	Precession rate, $\dot{\varpi}$ (deg day^{-1})	Inclination, i (deg)	Long. of ascending node,[c] Ω (deg)	RMS (km)
7	Unweighted; nominal parameters	140220.6 ± 1.9	2.61 ± 0.06	-0.38 ± 0.17	22.3 ± 1.2	2.6995 ± 0.0003	0.0035 ± 0.0012	30.9 ± 11.4	4.1
8	Weighted; nominal parameters	140222.2 ± 4.0	2.57 ± 0.18	-0.17 ± 0.68	22.9 ± 4.2	2.6998 ± 0.0013	0.0049 ± 0.0056	19.9 ± 25.1	7.3
9	Weighted; $T = 18$ year, $t_0 =$ Feb 1994	140223.4 ± 4.9	2.52 ± 0.17	$+0.03 \pm 0.69$	24.1 ± 2.2	2.7001 ± 0.0008	0.0067 ± 0.0040	13.6 ± 7.5	9.3
10	Weighted; $T = 20$ year, $t_0 =$ Feb 1994	140221.8 ± 3.3	2.60 ± 0.20	-0.30 ± 0.69	21.3 ± 5.3	2.6994 ± 0.0015	0.0032 ± 0.0057	35.3 ± 76.3	5.8
11	Weighted; $T = 19.08$ year, $t_0 =$ Feb 1992	140226.0 ± 5.6	2.89 ± 0.59	-0.59 ± 0.93	14.8 ± 10.8	2.6978 ± 0.0027	0.0051 ± 0.0106	134.2 ± 86.3	7.4
12	Weighted; $T = 19.08$ year, $t_0 =$ Feb 1996	140226.3 ± 10.8	2.59 ± 0.25	$+0.27 \pm 0.88$	21.3 ± 8.6	2.6996 ± 0.0018	0.0058 ± 0.0011	28.1 ± 42.4	8.3

[a] Fit identifier numbers are continued from Table III.

[b] "Nominal" parameters are taken from Murray and Giuliatti Winter (1997); they include period $T = 19.08$ yr and close approach time $t_0 = 4$ February 1994. In the weighted fits, weights are assigned as $(drms)^{-2}$, where dataset RMS ($drms$) is listed in Table II for each data set.

[c] Longitudes are measured in the J2000 system, from the intersection of the planet's equatorial plane with the Earth's. The reference time is the J2000 epoch.

for 1995/HST and 1995/IRTF to 0.01 and 0.17 km, respectively. These data are the most sensitive to inclinations, yet have the largest dataset RMS residuals (from circular features); the fit trades off a small change in inclination for a larger change in eccentricity parameters. Given the relatively low spatial resolution of these 1995 data due to the nearly edge-on viewing geometry, fit residuals less than 1 km are unrealistic. To remedy this situation, for the remainder of the fits we weight each data point using the "dataset RMS," that quantity given in Table II, which describes the RMS residuals for the circular features in the dataset. Fit #8 in Table IV is the result of a weighted fit with period and reference time fixed at MGW96 parameters. Here, the eccentricity amplitude is statistically insignificant.

We test the effect of MGW96's values for period and reference time on our fits by performing fits #9–12 in Table IV. First we change the period by ± 1 year, next the reference time by ± 2 years. In no case do we obtain a statistically significant value for eccentricity amplitude. Note also that the fitted values of h_e are in many cases much larger than the MGW96 predicted value of 0.155×10^{-3} (as well as the Borderies *et al.* (1983) value of 0.26×10^{-3}) and therefore are not entirely consistent with the variable eccentricity model. Thus, for a range of periods and reference times near MGW96's predicted values, the occultation data are consistent with a constant eccentricity. Therefore, Fit #3 in Table III remains our best solution for the kinematics of the F ring. However, because the ring inclination is determined mainly by the 1995 data, and inclinations can trade off with other effects, we multiply the stated uncertainty in the ring inclination and node location by a factor of 2 to account for this unknown amount of external error. Thus, our final value for the F ring's inclination is 0.0065 ± 0.0014 degrees and for the node is 16.1 ± 7.2 degrees.

Densities of Prometheus and Pandora

When we allow for secular perturbations by the satellites, the precession rate of the F ring is calculated to be 2.7004 deg day^{-1}. This calculation assumes a density of 0.65 g cm^{-3} for Prometheus and Pandora, the same value as was measured for Janus and Epimetheus (Nicholson *et al.* 1992). Prometheus' contribution to the secular component is greatest (66% of the satellite total), followed by those of Pandora (13%) and Titan (7%). The total satellite contribution is 0.002347 degrees day^{-1}. This predicted value is in line with the fitted precession rate using occultation data, 2.7001 ± 0.0004 degrees day^{-1}. Although it does not place a strong constraint on the masses of the shepherd satellites, we find that a density similar to that of the nearby coorbitals is consistent with our analyses.

4. ECLIPSES AND OCCULTATIONS

Our adopted inclination for the F ring of 0.0065 ± 0.0014 deg (2σ) amounts to a maximum displacement of ~ 16 km above or below the mean ring plane. This leads to two interesting consequences: when the subsolar latitude on Saturn (B') is close to zero, the F ring can be eclipsed by Saturn's A ring (which is assumed to lie in the mean ring plane), and when the sub-Earth latitude (B) on Saturn is near zero, the F ring can be occulted by the main rings and can in turn occult part of the main rings itself. The specifics of both effects—where and when the eclipse or occultation will be seen—depend on the location of the node (Fit #3 in Table III). We consider these effects at the four epochs of Earth or Sun crossing events: 22 May 1995 (Earth crossing), 10 August 1995 (Earth crossing), 21 November 1995 (Sun crossing), and 12 February 1996 (Earth crossing).

Ring-to-Ring Eclipse

Near the solar ring-plane crossing, the A ring can eclipse the inclined F ring. Images of the Saturn system taken shortly after the 1995 stellar occultation capture this effect and thus provide independent confirmation of the inclination (Fig. 4). In Fig. 5 we plot the height of the F ring from the mean ring plane; the region eclipsed by the A ring is indicated by the heavy line. The adopted orbit model predicts the F ring to be in eclipse from 110.9 (+3.2, −1.7) degrees to 219.2 (+8.2, −9.3) degrees (2σ) from the sub-Earth point, where the uncertainty is a result of

FIG. 5. Predicted eclipse of Saturn's F ring by the A ring on 22 November 1995. The height of the F ring above the mean ring plane is given, along with the region of the A ring shadow (area within heavy dashed line). Longitude is measured prograde from the sub-Earth point. Based on the inclined model for the F ring, the eclipse is predicted to occur at the intersection of these two lines; the eclipsed segment of the F ring is indicated in bold. The predicted eclipse region spans longitudes from approximately 111 to 219 degrees. The eclipse on the west ansa is observed in WFPC2 images at 111.5° (dot–dash vertical line). To estimate the effects of the F ring's vertical thickness on eclipse location, the shaded region around the F ring's core represents a full thickness of 5.6 km, while the dotted lines within represent a full thickness of 2.0 km.

the adopted uncertainty in the inclination and node (twice the formal errors). The observed west-ansa dimming of the F ring in Fig. 4 occurs at 111.5° from the sub-Earth point, approximately the same location as predicted by the inclined F ring orbit model (Fig. 5). The expected east-ansa brightening is not as obvious as is the dimming on the west ansa. The F ring's brightness does change near the predicted east location; this is easiest to see by comparing the brightnesses of the F ring and the Cassini Division along the features. However, the F ring is still visible from the Saturn shadow to the predicted emergence point, although it should be eclipsed by the main rings in this region. An uncertainty in the predicted emergence longitude of ∼8 degrees follows from the adopted uncertainty in the longitude of the node; however, this is not enough to move the predicted emergence longitude into the Saturn shadow. Its visibility may be due to its vertical thickness, vertical oscillations along the ring, and/or vertical warping of the A ring. The actual behavior will depend on the local behavior of the longitudinally asymmetric ring and on the vertical distribution of ring particles with respect to distance from the mean ring plane. To show the differences among several possibilities, we choose two values of vertical thickness to illustrate in Figs. 5 and 6.

A thickness of ∼5 km, which is ∼4 times the photometric thickness measured by Bosh *et al*. (1997), leads to a gradual brightening on the east side, one that begins within the shadowed region and continues for about 20° in longitude. Similarly, the west side disappearance into eclipse would not occur instantaneously, but would occur over ∼4°, a much smaller region due to the steeper angle of the A ring shadow at this location. A smaller value of ∼2 km, which is the FWHM of the 1995

FIG. 4. Saturn's rings from 22 November 1995, approximately 31 hours after the occultation of GSC5249-01240. We obtained a series of four images (two of each ansa) with the Wide Field/Planetary Camera 2 on HST. The two images taken at each ansa have been combined to remove cosmic ray hits; as a result, satellites and stars (i.e., beneath ring on east ansa) are partially removed along with the cosmic rays. Brightness levels and contrast were adjusted equally for east and west subimages. On the east, the shadow of the planet on the rings is visible. These data were obtained just after the ring-plane crossed the Sun, therefore we are viewing the unlit face of the rings. In this unusual view, the bright ring regions are areas where sunlight is transmitted through optically thin ring material, the opposite of the more normal view of sunlight reflected off the rings. Arrows indicate the predicted eclipse locations, based on the inclination and longitude of the node determined from the geometric fit. The uncertainty in the eclipse location due to the 2-σ fitted uncertainties in inclination and node longitude is represented by the line above each predication location. Due to the geometry of the A ring shadow (Fig. 5), the uncertainty is much larger on the east ansa than it is on the west ansa. For a ring with significant vertical thickness, the behavior on emerging from eclipse will be gradual brightening, over a distance that is approximately the same as the uncertainty length, if the total thickness of the ring were ∼5 km.
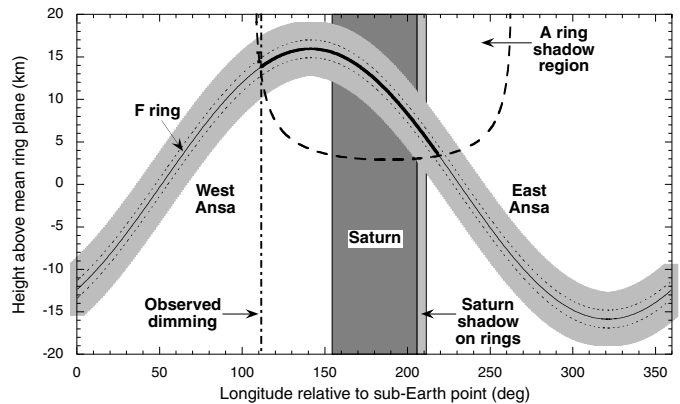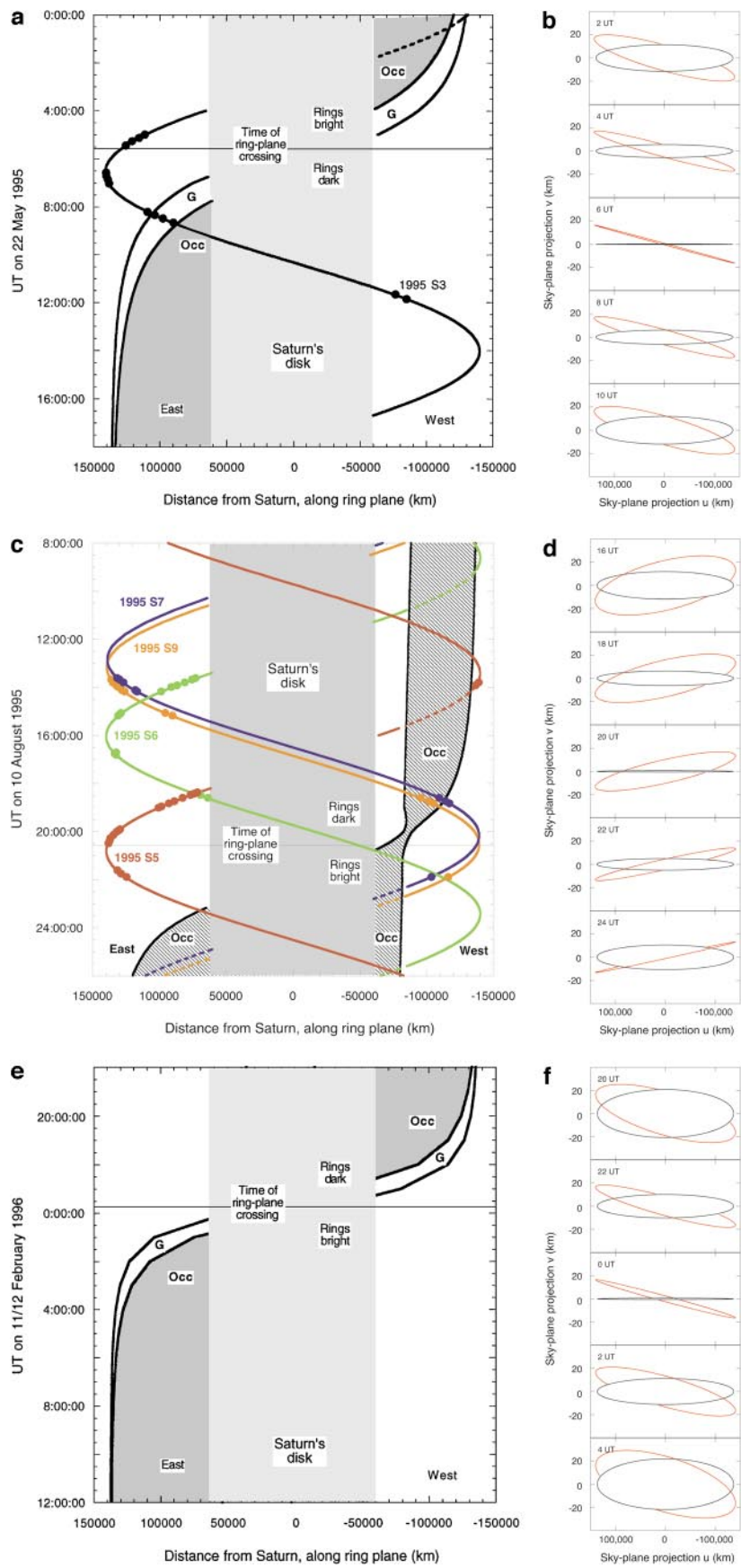
occultation profile times sin B, results in similar behavior over shorter distances. Both thickness scenarios are shown in Fig. 5, while only the 5-km scenario is shown in Fig. 6.

Ring-to-Ring Occultation

In May and August 1995 and February 1996, as the Earth crossed Saturn's ring plane, the small opening angle B and resulting foreshortening of the rings along the line of sight allows occultations by and of the F ring. The visibility of the F ring is dependent on the location of the node at the time; we display this for each ring-plane crossing epoch in two ways in Fig. 6. In the left-side panels (Figs. 6a, 6c, 6e) we plot distance from the center of Saturn on the sky plane as a function of time. Circular or near-circular orbits appear as sinusoidal curves in this geometry. Shaded regions depict areas where the F ring is occulted on the far side of the rings (labeled "Occ"), and the transition region where a ∼5-km thick ring would gradually go into occultation (lightest fill, between two heavy lines, labeled "G" for gradual). The right-side panels show cartoons of the ring geometry during each epoch, with the F ring in red and the main rings (represented by the outer edge of the A ring) in black. The sky plane coordinates u and v are described in Elliot *et al.* (1993). During the May and February crossings, the line of nodes was almost coincident with the line of sight, so that at the time of crossing the region in which the F ring is occulted by the main rings is mostly hidden from view behind the planet (Figs. 6a, 6b, 6e, 6f). In both May and February, part of the F ring is obscured during the time when the rings are dark, just after or before crossing. In August, however, the situation is different (Figs. 6c, 6d): 80 days later than the May crossing, the ascending node has regressed by $215°$ and now lies on the near side of the East ansa. In this region, the F ring passes in front of the main rings, partially obscuring them. Whether or not this is noticeable as a reduction in flux depends on photometric models for the surface brightness of the rings, and this question will not be pursued here. Before the ring-plane crossing at ∼21^h UT, the F ring is occulted by the main rings just after it rounds the west ansa and remains blocked until very close to its descending node when it reappears (Figs. 6c, 6d).

Observational Implications

During these ring-on-ring occultations, any satellites/clumps traveling in or near the F ring, with the same inclination and node as the F ring, will be hidden from view when the F ring is occulted by the main rings. In the left-side panels of Fig. 6,

possible F ring clumps are included (McGhee *et al.* 2001). For some of these clumps, it is unclear whether they are part of the F ring or orbit separately from it. If these are indeed in the F ring, they will also be occulted when the F ring is occulted. When these bodies are in the occultation zones, their orbital paths are indicated by dashed lines. In August, the node position results in significant obscuration of the F ring on the west ansa. At least one clump fell prey to this occultation zone in August. 1995 S5, discovered during the August crossing (Nicholson *et al.* 1996), appears to orbit within the F ring or just interior to it. If we assume that it has the same orbital plane parameters as the F ring, it should have disappeared from images taken between 14:10 and 15:30 UT. During this time, at least two groups were observing the rings, with the HST (Nicholson *et al.* 1996) and with a ground-based adaptive optics (AO) system (Roddier *et al.* 2000). The HST team reports two detections of S5 on the west ansa, obtained at 13:47 and 13:54 UT (included in Fig. 6c), just outside the occultation zone (and thus visible). The AO group reports 42 images obtained between 14:33 and 15:19 UT with no detection of S5 during this time, consistent with our analysis. S5 does appear in an additional 49 AO images obtained between 12:10 and 12:56 UT (not included in Fig. 6c), outside the window in which it would have been in occultation. The lack of detection in the 14:33–15:19 UT AO images suggests that S5 is a clump within the F ring, or if it is an independent satellite, that its node happened to be coincident with or is locked to the F ring's; otherwise differential regression would separate them.

As a result of these F ring occultations, the inclination of the F ring must be considered when interpreting the images taken during ring-plane crossings, both for clump tracking and for ring photometry. Analysis of the August 1995 ring-plane crossing showed different times of minimum ring flux for the east and west ansae (Nicholson *et al.* 1996). As the F ring contributes most of the flux during this edge-on configuration, accurate photometric modeling (including occultation of the F ring by the A ring and vice versa) will be necessary to determine if the timing difference can be attributed to the inclination of the F ring (Nicholson *et al.* 1999).

5. PARTICLE SIZES

Detailed studies of Saturn's F ring are complicated by this feature's proximity to the bright main rings. Therefore, most work has been done using spacecraft data (Pioneer 11, Voyagers 1 and 2) and/or stellar occultation data. An investigation of statistical

FIG. 6. Occultations of the F ring by the A ring. For the Earth ring-plane crossing epochs of May 1995, August 1995, and February 1996, panels a, c, and e show the regions in which the F ring is occulted. The schematic diagrams in panels b, d, and f show the orientation of the node at the same epochs. In the left-side panels, the darker fill area labeled "Occ" indicates the region in which the F ring is completely occulted by the A ring, while the light fill area (labeled "G" for gradual) represents the region over which a 5-km thick ring (or clump) would gradually disappear behind the A ring. The August 1995 plot (panel c) includes only the nominal disappearance times to reduce clutter. In these panels, orbit plots and individual measurements for suspected F ring clumps are also given. When the path of one of these bodies takes it into A-ring occultation, the line is changed from solid to dashed. When in front of the rings (closer to Earth than the main rings), the F ring and any clumps will not be occulted, therefore some lines are solid although they cross occultation zones. No clumps were observed within the occultation zones.

fluctuations in the Voyager 2 PPS occultation data was used to set an upper limit of approximately 2 m on particle sizes in the F ring (Showalter and Nicholson 1990). Analysis of 69 Voyager images of the F ring taken at phase angles ranging from 7° to 156° points to dust as the major component of the F ring: particles roughly 0.03 to 1 μm in radius are believed to be responsible for the observed scattering behavior (Showalter *et al.* 1992; hereafter S92). S92 modeled the phase curve with two populations of water ice particles (small and large), using a modified Pollack and Cuzzi (1980) method for nonspherical, randomly oriented particles. S92 then compared this phase curve result with equivalent depth measurements from two occultation data sets: Voyager 1 RSS (X- and S-bands) and Voyager 2 PPS (δ Sco). The radio (RSS) equivalent depth is much smaller than that for the shorter wavelength PPS data; they interpret this as due to larger, cm-sized particles. Because the RSS data show no evidence of a wide envelope as do the PPS data, S92 postulate that the large particles dominate the narrow core, while μm-sized particles dominate the envelope.

An issue in combining different occultation data sets is the possibility of change along the ring or over the time between observations. Evidence for longitudinal brightness variations exists in images from Voyager (Fig. 1 in Kolvoord *et al.* 1990) and from Earth-based ring-plane crossings (Fig. 7 in Nicholson *et al.* 1996; Fig. 12 in McGhee *et al.* 2001). These brightness changes may be due to transient clumps (Showalter 1994, Showalter 1996) or gravitational interactions with nearby perturbing satellites (Showalter and Burns 1982, Lissauer and Peale 1986, Kolvoord *et al.* 1990). Time-dependent differences may be present in the F ring, as it was predicted to have collided with Prometheus in
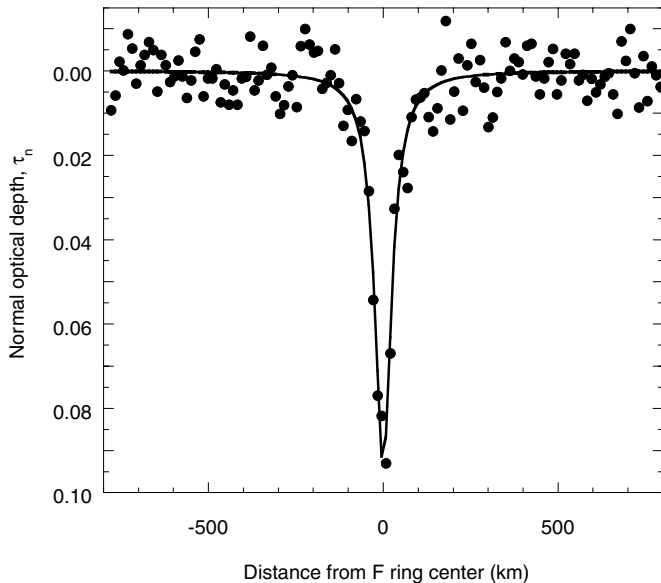

FIG. 7. Representative fit of Lorentz function in ring-plane radius to normal optical depth values at one wavelength bin (diode 150, 0.41 μm). Fit parameters include area under the curve A (equivalent depth), full width at half maximum Γ, and feature center r_0.

1994 (MGW96); although whether or not this occurred is now in question (Section 3, this work). If a collision did occur in the early 1990s, it may have changed the character of the ring between the epochs of Voyager and the 1995 occultation measurements.

The data from the 1995 occultation of GSC5249-01240 observed with the HST's FOS are unique because they provide simultaneous multi-wavelength information on the same portion of the ring. We investigate the dependence of equivalent depth A on wavelength to infer properties of the particle size distribution within the F ring. We first describe our method for calculating equivalent depths and then discuss possible explanations for the observed distribution with wavelength.

Equivalent Depth

The equivalent depth of a nonopaque ring, A, is the radially integrated normal optical depth, $\int \tau_n(r)\,dr$, and is a measure of the abundance of ring material (Elliot *et al.* 1984). To obtain calibrated normal optical depths, τ_n, versus radius r in the ring plane, we first remove the varying background signal—scattered light from Saturn and light transmitted through the rings—that is present in the occultation data. We perform a linear fit to the signal levels near the F ring, approximately 800 km outside the F ring to just inside the Encke gap. All sharp transitions are ignored for background fitting. We calculate the unocculted stellar signal f_0 from the drop at the outer edge of the A ring; because the opening angle B is small, the A ring is opaque in these data. On a small scale such as this, a simple linear fit is appropriate and higher order polynomials are not needed. We calculate the normal optical depth using $\tau_n = -\sin B \ln(f/f_0)$ for each observed background-subtracted signal level f. For this event, $\sin B = 0.047$. We next fit an area-normalized Lorentzian function to the calculated values of τ_n (Fig. 7),

$$\tau_n(r) = \frac{A}{\pi} \frac{\Gamma/2}{[(\Gamma/2)^2 + (r - r_0)^2]}, \qquad (2)$$

where Γ is the full-width at half maximum of the distribution, A is the area under the curve and is equal to the equivalent depth, and r_0 is the center of the distribution. We fit for these Lorentz parameters for every diode (wavelength step) in our data (Fig. 8). The signal-to-noise ratio per diode is considerably less than for the wavelength-binned data in Fig. 1c, in part because we immediately lose much of the signal by dropping the zeroth-order spectrum (Fig. 1a). In addition, the noise is greater at the short and long wavelength ends of the spectrum; this is visible in Fig. 8 as increased scatter at extreme values of wavelength.

The significant feature of Fig. 8 is the lack of a strong wavelength dependence of any of the parameters. The unweighted mean value of A over the wavelength range is 7.41 ± 0.15 km. If we assume a linear dependence on wavelength, we can place an upper limit on the slope $\partial A/\partial\lambda$ from a least-squares fit: -1.36 ± 1.43 km μm^{-1} (1σ). Thus, these data suggest that the
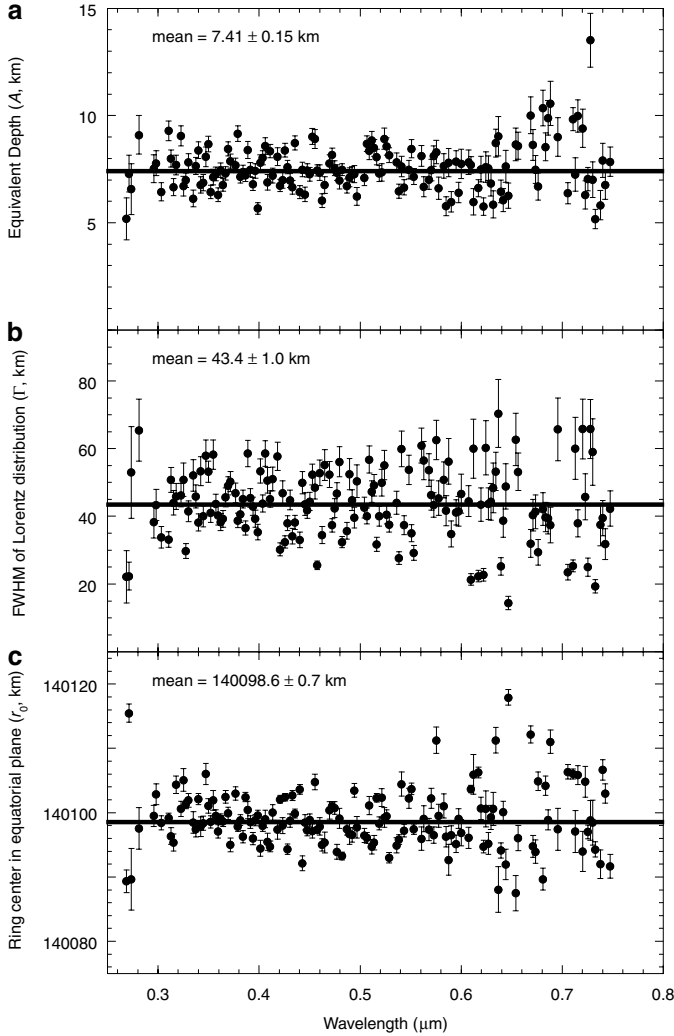
FIG. 8. Full results of Lorentz fit to F ring data versus wavelength. (a) Equivalent depth A, (b) full width at half maximum Γ, and (c) distribution center r_0. The mean is given for each and is indicated by a heavy horizontal line. All quantities are approximately constant with wavelength, an observation that is used to constrain particle properties within the F ring.

equivalent depth is constant over the wavelength range 0.27–0.74 μm. Comparison values for equivalent depth from other occultation datasets are given in Table V.

Particle Size Distribution Retrieval

Occultations by narrow, isolated rings primarily measure extinction of the direct beam by the ring particles; the amount of extinction suffered by starlight as it passes through the ring depends on the number density of particles and on their sizes, shapes, and compositions. The normal optical depth τ_n of a ring is related to the size distribution of particles within it by

$$\tau_n(\lambda) = \int_{a_{\min}}^{a_{\max}} n(a)\pi a^2 Q_e(a, \lambda)\, da, \qquad (3)$$

where a is the particle radius, $a_{\min}$ and $a_{\max}$ are lower and upper size limits on particles, $n(a)$ is the differential number density of particles of that radius per unit area, and Q_e is the extinction efficiency at wavelength λ. The factor Q_e describes how much light a particle blocks relative to its physical cross section and depends on wavelength, particle size, and particle composition. If the particle is much larger than the wavelength (geometric optics limit), $Q_e \rightarrow 2$. This occurs because the particle diffracts an amount of light equal to the amount it absorbs or reflects, and this diffracted light is then considered to be removed along with the light directly blocked by the particle. In addition, Cuzzi (1985) replaces Q_e with $Q_e(occ)$, a factor that accounts for a replaced diffracted component—that is, some of the light that was diffracted out of the beam can be replaced or diffracted back into the beam if the star is large enough or from other sections of the ring. This factor depends on the diffraction angle $\theta_d \approx \lambda/2a$, the distance of the observer from the ring, and the width of the ring. For ground-based occultation data on narrow rings, $Q_e(occ) \rightarrow Q_e$ unless θ_d is smaller than the angular diameter of the star; for the 1995 occultation this occurs only for particles larger than about 2 km. Thus, by assuming particles smaller than this, we can ignore the replaced-diffracted component and use Q_e rather than $Q_e(occ)$.

The extinction efficiency Q_e is a function of wavelength λ, particle size a, and complex index of refraction, $m = n - ik$ (the imaginary portion, k, describes the absorption). Therefore, we must know the particle composition to choose an appropriate index of refraction. Water ice has been identified in Saturn's rings (Kuiper *et al.* 1970, Lebofsky *et al.* 1970, Pilcher *et al.* 1970, Clark 1980); it is believed that there is an additional contamination component (Estrada and Cuzzi 1996), but for this analysis we assume it is negligible. For water ice at approximately 75 K (Grundy *et al.* 1999), we use refraction coefficients from Warren (1984). For wavelengths 1–2.7 μm we use more recent coefficients from Grundy and Schmitt (1998). In the visible wavelength range of the HST FOS observations, the index of refraction is approximately $m = 1.3 - i10^{-8}$ (Fig. 9). We calculate the extinction efficiency for a collection of spherical particles rigorously from Mie theory (van de Hulst 1981). In Fig. 10a we plot Q_e against size parameter $x = 2\pi a/\lambda$ for water ice spheres at a constant wavelength of $\lambda = 0.5$ μm. We suppress the smallest scale "ripple" structure (± 0.15 in Q) in this figure because it is unobservable in these data. The abscissa of this graph is a function of both a and λ, and thus Fig. 10a is not appropriate for all wavelengths because the optical constants may vary with wavelength (Bohren and Huffman 1983). To emphasize this point, we present in Fig. 10b Q_e plotted against x at a constant particle size of $a = 0.5$ μm. The "extra" features at low x values in Fig. 10b as compared to Fig. 10a arise due to the infrared absorption of ice, and the sudden flattening at $x \sim 20$ is due to the UV ice absorption edge (Fig. 9).

van de Hulst (1981, Table 15, p. 178) notes that the location of the first maximum in $Q_e(x)$ is near $2x = 4.1/|m - 1|$. For our values of refractive index, the first maximum or turnover occurs

TABLE V
F Ring Optical Depth

UT Date	Event	Station	Wavelength	Equivalent Depth[a] (km)
1995 11 21	GSC5249-01240	HST	0.27–0.74 μm	7.41 ± 0.15
		IRTF	2.30 μm	5.76 ± 0.06
1989 07 03	28 Sgr	IRTF (egress)	3.10 μm	3.79 ± 0.08
		Palomar (ingress)	3.9 μm	3.0 ± 0.1
		McDonald (ingress)	2.1 μm	2.8 ± 0.1
		McDonald (egress)	2.1 μm	3.6 ± 0.1
1981 08 26	δ Sco	Voyager 2 PPS	0.26 μm	4.33 ± 0.13
1980 11 13	Voyager 1 RSS	DSS-63	3.6 cm	0.283 ± 0.035
1980 11 13	Voyager 1 RSS	DSS-63	13 cm	0.153 ± 0.066

[a] Equivalent depth (A) values for Voyager 2 PPS and Voyager 1 RSS data are taken from Showalter *et al.* (1992); values for 28 Sgr Palomar and McDonald are from P.D. Nicholson *et al.* (private communication).

near x of 6.8; for a wavelength of 0.5 μm, this corresponds to particles $\sim$0.5 μm in radius. Therefore, if there were significant numbers of particles roughly 0.1–0.5 μm (smaller than 0.1 μm scatter too inefficiently to impact τ), these 1995/HST data would show a nonzero slope $\partial A/\partial \lambda$. Instead, A is constant with wavelength over the range 0.27 to 0.74 μm (Fig. 8a).

A collection of spherical water ice particles of a single size is unlikely for the F ring. In reality we expect a range of particle sizes and contaminants to be present in or on the ice, and particle shapes to be more irregular than spheres. These effects will alter the dependence of A on wavelength. We begin by exploring the particle size distribution (PSD). A PSD of the form
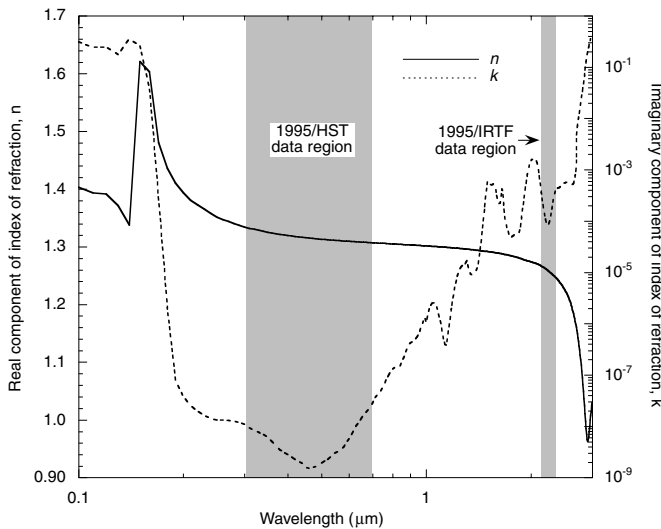
$$n(a) = n(a_0)\left(\frac{a_0}{a}\right)^q \quad (4)$$

has often been used to describe ring particle sizes. Here, a_0 is a reference particle size and q is the number density power. For typical fragmentation processes expected in the rings, q is between 3.0 and 3.5 (Hartmann 1969, Greenberg *et al.* 1977). For Saturn's A ring with particle sizes 1–100 cm, $q \sim 3.4$ (Zebker *et al.* 1985; Marouf *et al.* 1986). S92 find $q = 4.6 \pm 0.5$ for the F ring, with particle sizes 0.03–1 μm.

Combining the equations for A and τ_n, we find

$$A \propto \int \int_{a_{\min}}^{a_{\max}} a^{2-q} Q_e(a, \lambda)\, da\, dr \quad (5)$$

FIG. 9. Complex index of refraction ($m = n - ik$) versus wavelength for water ice at 75 K. Values are from Warren (1984) and Grundy and Schmitt (1998). The approximate wavelength regimes of the two 1995 occultation datasets are indicated by the shaded areas. Note that the ordinate for the real component n is linear while that for the imaginary component k is logarithmic.
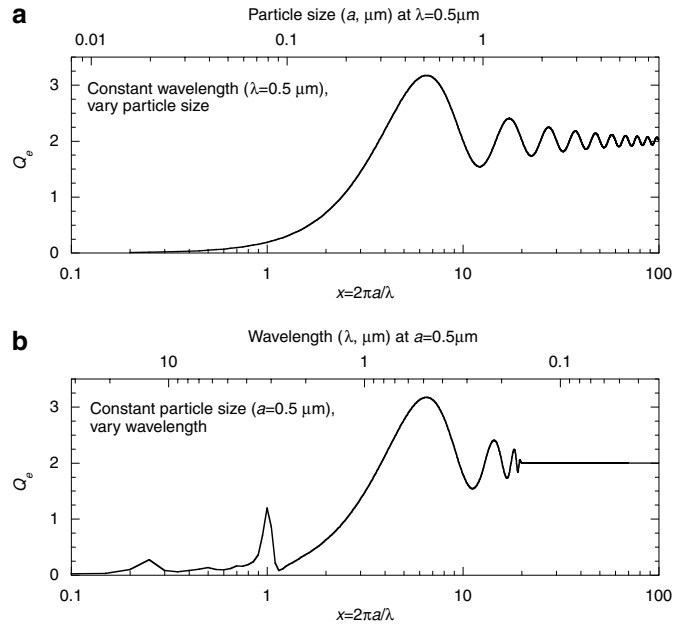
FIG. 10. Extinction efficiency Q_e for water ice spheres calculated from Mie theory. The abscissa is the size parameter x, the ratio of the particle circumference to the wavelength. (a) Q_e at constant wavelength, the particle size a varies. (b) Q_e at constant particle size, the wavelength λ varies. Because the index of refraction m depends on the wavelength, the shape of the curve is altered from that in (a). In our calculations, we take into account the dependence of index of refraction on wavelength.
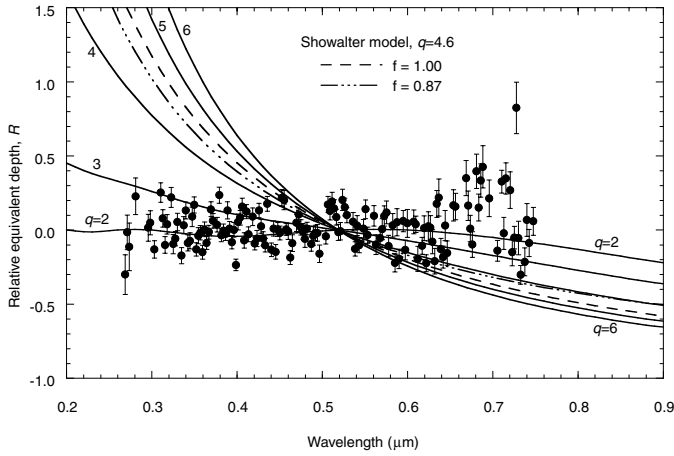
FIG. 11. Relative equivalent depth $R = [A(\lambda) - \langle A \rangle]/\langle A \rangle$ for F ring observations and models. The mean value of equivalent depth, $\langle A \rangle$, is 7.41 ± 0.15 km. Showalter *et al.* (1992) models with small-particle fractions of 100% and 87% are plotted as the dashed and dot–dashed lines. We explore different number density powers q in additional models. For all models, $a_{\min} = 0.03$ μm and $a_{\max} = 1$ μm. Models are normalized to A value at a wavelength of 0.52 μm, the approximate center of our range.

Therefore, the variation of A with wavelength depends on both the extinction efficiency and the PSD. In PSDs with small values of q ($\lesssim 3$), the large particles contribute significantly to the extinction. When q is larger, the relatively larger numbers of small particles control the scattering and extinction. We test models by comparing the Q_e spectrum against our data. We compute the relative equivalent depth, R,

$$R(\lambda) = \frac{[A(\lambda) - \langle A \rangle]}{\langle A \rangle}, \qquad (6)$$

where the reference equivalent depth $\langle A \rangle$ is the mean of A from the 1995/HST data. This function has the advantage of removing the dependence on unknowns such as the number of particles at the reference size $n(a_0)$. In Fig. 11, we plot our values for relative equivalent depth R with models representing various values of q. The S92 value of q, 4.6 ± 0.5, is incompatible with the 1995/HST data. This is not a completely fair comparison, as the S92 model used irregular, randomly oriented particles, whereas the models in Fig. 11 are calculated using Mie theory for perfect spheres. However, it is interesting to note that in this idealized case, a lower value for q is suggested by the data.

Other factors that affect the shape of the Q_e curve (and therefore the R curve) are the upper and lower size cutoffs. With so many free parameters, plots such as Fig. 11 quickly become cluttered. Instead, we calculate the maximum absolute value of the relative equivalent depth slope $\partial R/\partial \lambda$ for each model. We use the maximum value of the slope in the wavelength range rather than the average value of the slope calculated from values at the two endpoints because we found that these other methods were not good measures of the true variability within the region. From an unweighted fit to the 1995/HST data, the slope is $0.23 \pm$

0.16 μm^{-1} (1σ). For the models we calculate R at every 0.02 μm in wavelength between 0.3 and 0.7 μm, and take the maximum absolute value of the slope from these values. In Fig. 12 we compare various models with the observed 2σ upper limit on the slope of 0.55 μm^{-1} and explore the effects of different upper and lower cutoffs. In Fig. 12a, $a_{\max}$ is 1 μm, while in Fig. 12b the value is 2 m. We take the value of 2 m for $a_{\max}$ from Showalter and Nicholson (1990), but the exact value has little effect on the result as long as it is larger than approximately 10 μm (the size near which the Q_e curve becomes flat; Fig. 10). Within each plot, different line styles indicate $a_{\min}$ values of 0.1, 0.2, and 0.5 μm. The 2σ upper limit to the slope imposed by the 1995/HST data is indicated in each plot by a heavy horizontal line. Thus, models that are consistent with the 1995/HST data lie below this line. The result of S92 for q is indicated by vertical lines ($\pm 1\sigma$). The shaded intersection of these two areas will apply if the phase angle analysis of S92 is applicable to our observations.

In Fig. 12 one immediately notices that many of the curves lie entirely above the intersection region and therefore are inconsistent with the 1995/HST data. No model with $a_{\max} = 1$ μm
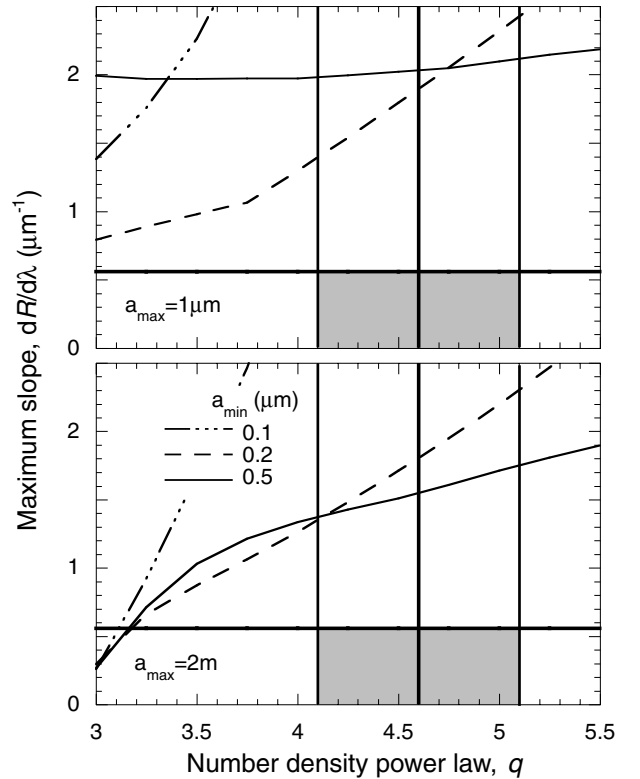

FIG. 12. F ring particle size models, with 1995/HST constraint. The invariability of the 1995/HST data with wavelength constrain possible models for particle size distribution within the ring, as model values for relative equivalent depth R may change appreciably in the observed wavelength range 0.3–0.7 μm. Changes in various model parameters are explored and are compared with the low-slope constraint from the 1995/HST data (2σ upper limit to slope of 0.55 μm^{-1}, indicated by the bold horizontal line in each panel). For the top panel $a_{\max} = 1$ μm, and for the bottom panel $a_{\max} = 2$ m. Within each panel, line styles indicate $a_{\min}$ of 0.1, 0.2, and 0.5 μm (see bottom panel for key).

is consistent with the data; the particles are too small so their Q_e values vary too much within the wavelength range 0.27–0.74 μm. By adding larger particles (increasing a_{max} to 2 m), the variations in Q_e are modulated and some a_{min} values fall into the consistent region. However, at $a_{max} = 2$ m, only PSDs with q values less than 3.2 are allowed. Notice that at $a_{max} = 2$ m, the minimum particle size a_{min} is not well constrained; any size particles 0.1–0.5 μm fit equally well for similar values of q.

Another option for a PSD that has been suggested is a combination of 2 PSDs: one with predominantly small particles, another with predominantly large particles. Given the constancy of the observed values of A in our wavelength range, we cannot constrain such a combined distribution, but we can place an upper limit on the relative populations. The fraction of small particles (smaller than $\sim$1 μm) present at this location in the F ring would need to be less than $\sim$28% to be consistent with the observed data. We approximate this by using the top panel of Fig. 12, choosing an S92-type distribution and taking the value of the slope as $\sim$2, the smallest value for $q = 4.6$.

Additional model refinements are possible by changing the absorption to account for contaminants or by including the effects of nonspherical particle shapes. However, these produce only subtle changes in the models, and adding such complexities is not warranted by the data.

If we could add other constraints we could restrict the possible solutions for PSDs. However, due to the F ring's variability, constraints from other epochs cannot be used in conjunction with the 1995/HST constraint. The constraint from the 1995/IRTF data set cannot be applied because the corotating longitude sampled by the IRTF datum is far removed from that of the HST datum (Table II). Therefore, the 1995/HST constraint stands alone, suggesting particles with $q \sim 3$, and 10 μm $< a_{max} < 2$ m. A model with $q = 3$, $a_{min} = 0.1$ μm, and $a_{max} = 2$ m is presented in Fig. 13. Note that the predicted value for R at 2.2 μm is larger than the observed IRTF value, suggesting longitudinal variability within the ring.

6. PHYSICAL DESCRIPTION OF THE F RING AND ITS ENVIRONS

The Width of the F Ring

In the δ Sco/PPS stellar occultation profile (Fig. 2), the core of the F ring is a very narrow feature, less than 1-km wide, while the total width including the envelope is approximately 50 km. The optical depth of the core in the PPS dataset is a factor of several larger than the wings. In contrast, the FWHM of the 28 Sgr profiles are 18–24 km (Nicholson, 2000); these were interpreted as due to the 18-km diameter of the star. In the 1995 data, we find a FWHM of 43.4 ± 1.0 km for 1995/HST (Figs. 7 and 8b) and 44.7 ± 0.7 km for 1995/IRTF. If this radial width were due to convolution with a stellar profile, the star would be $\sim$7 km in diameter (its projected size on the sky plane at Saturn). However, this size is inconsistent with the magnitude and assumed solar spectral type of this star, which suggest a projected diameter of only 0.15 km. It is also inconsistent with the sharp diffraction spikes at the outer edge of the A ring and on both edges of the Keeler and Encke gaps (Fig. 1c); these spikes would not be present with this morphology if the star were $\sim$7 km across.

Given the oblique viewing geometry ($B \sim 3°$) of the 1995 occultation, the measured ring width is most likely a combination of radial width and vertical thickness of the F ring. During the geometric analysis of occultation data (conversion from observed time to ring-plane radius), we assume that all features exist in an infinitesimally thin ring plane. When mapped onto the ring plane, the significant vertical extent of the F ring is increased by a factor of $\sim$21 for the 1995 event. Thus, the geometrically derived width of 43 km corresponds to just 2 km in vertical thickness. The actual thickness may be larger than this because the total width of the ring is much larger than its FWHM. Using a criterion of enclosing 95% of the total Lorentz distribution, the total extent of the F ring in Fig. 7 is 275 km. If this is all attributed to vertical direction, the ring could extend over 13 km vertically.

Dust Sheet between A and F Rings

A tenuous sheet of material between the F and A Rings has been reported based on Voyager images. Burns *et al.* (1983) estimate τ_n of 10^{-4} to 10^{-5} from analysis of Voyager 2 images at phase angles of 41–43°. Following this discovery, Graps *et al.* (1984) performed a statistical analysis on Voyager 2 PPS occultation data and determined that material between the outer edge of the A ring and Atlas has τ_n of $(6–10) \times 10^{-3}$. Based on analysis of images obtained during the 1995 ring-plane crossing, Nicholson *et al.* (1996) placed an upper limit on τ_n of 2×10^{-5}. Most recently, Showalter *et al.* (1998) combine Voyager data at low (41–43°) and high phase angles (125–165°) to estimate $\tau_n = (1 - 2) \times 10^{-4}$ for a uniform sheet.
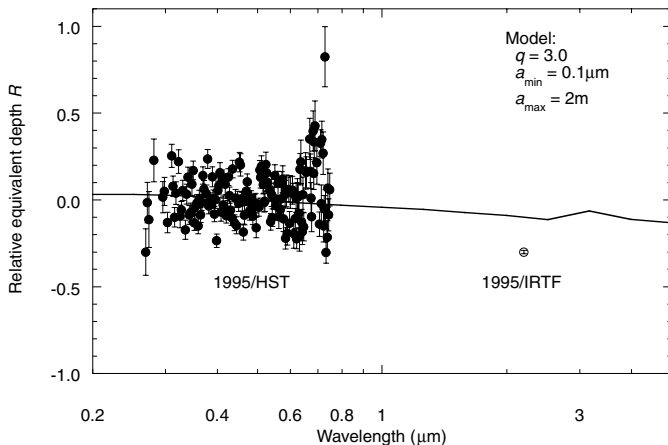

FIG. 13. One possible model for the F ring particles that is consistent with the 1995/HST data: $q = 3.0$, $a_{min} = 0.1$ μm, $a_{max} = 2$ m. Over the wavelength region 0.27–0.74 μm the model is approximately constant, as required by the 1995/HST data. Note that the 1995/IRTF datum, while from the same occultation event, falls significantly below the model value. This is indicative of the dramatic longitudinal variability within the F ring.

Inspection of the normalized signal from the 1995/HST occultation (Fig. 1c) reveals no high optical depth feature in the region between the F and A rings. We use these data to place an upper limit on any material existing in this region. Rather than remove background signal by assuming the regions just interior and exterior to the F ring are devoid of material, we instead assume that the region between the F and A rings may contain material. We then use the signal levels in the Encke gap (presumed empty), the region exterior to the F ring, and the region between the Keeler and Encke gaps to fit for full stellar flux and background levels. From these results we calculate the τ_n for each datum. From the mean and standard error of the mean in this region, we find a 3σ upper limit of 1×10^{-4} on the normal optical depth of a uniform dust sheet. This upper limit is in agreement with the previous measurements or upper limits described above, except for the Graps *et al.* (1984) result. Their statistical analysis refers only to a narrow region near the outer edge of the A ring. Such a band of material would have been visible in the 1995/HST data if present; therefore the Graps *et al.* feature is either an artifact or variable in time and/or longitude.

7. CONCLUSIONS

The 1995 occultation of GSC5249-01240, observed at 2.2 μm from IRTF and in a spectrally resolved mode from HST, provides a wealth of information about Saturn's F ring. By combining these data with previous occultation observations, we find an inclination of 0.0065 ± 0.0014 degrees (2σ) for the F ring. The maximum out-of-plane excursion is ~16 km, much greater than the Laplace plane warp (up to 300 m during the 1995 ring-plane crossing season; G. Black, private communication). This establishes the F ring as the first known inclined ring in the Saturn system. The F ring inclination is confirmed by HST imaging near the solar ring-plane crossing, which showed a dimming of the F ring as it entered eclipse by the A ring, at a longitude consistent with our model derived from occultation data. The origin of the F ring's inclination is unknown. Borderies *et al.* (1984) suggest that nearby satellites (such as Prometheus and Pandora) may excite an inclination in the F ring, which may be balanced against runaway growth by viscous dissipation. We note that the inclination of the orbits of Prometheus and Pandora have an upper limit of $0.1°$ (Synnott *et al.* 1983). Future ground-based observations of the F ring will not be as sensitive to inclinations as the 1995 occultation data, due to the increasing ring-plane opening angle. Therefore, refinements of the F ring's inclination await the Cassini spacecraft's arrival at Saturn in 2004.

The current data do not allow us to measure the predicted periodic variation in the eccentricity of the F ring because the data are too sparse. However, these data are consistent with a constant eccentricity. Because Saturn's rings are much larger than the Earth, observations of any one event do not provide a very strong constraint on eccentricity; however, observations from widely spaced observing stations on the Earth can provide

some constraint on eccentricity (Fig. 3). The 1989 28 Sgr event was widely observed and thus constrains the eccentricity at that epoch, but the coverage of other events is not dense enough to allow an independent determination of the eccentricity at other epochs. To remedy this situation, we must obtain more complete coverage of future occultation events.

The inclined F ring is subject to occultation by and of the main rings when observed near ring-plane crossing. This leads to implications for the interpretation of the 1995 observations of clumps and satellites in or near this ring. Depending upon the location of the node at the time, significant portions of the F ring may be hidden from view; any clumps orbiting within the ring would likewise be hidden. Analyses of previous and future crossing observations will need to consider these occultation zones; zone locations for the 1995–1996 ring-plane crossing season are shown in Fig. 6. Additionally, the fact that the F ring hides and is hidden by portions of the main rings has implications for ring photometry near crossing, particularly crossing time analyses (Nicholson *et al.* 1999). A photometric model including an inclined, optically thin ring will need to be developed to tackle this problem.

Through analysis of the spectrally resolved data from the occultation of GSC5249-01240 we find the equivalent depth of the F ring to be independent of wavelength over the range 0.27–0.74 μm. This result implies a ring for which much of the optical depth is in particles larger than about 10 μm, not the much smaller sizes (<1 μm) previously estimated (Showalter *et al.* 1992). This discrepancy may be due to time-variable behavior within this ring, or it may reflect an even greater degree of longitudinal asymmetry than was previously suspected.

Future Modeling Directions

A problem with particle size retrieval from multiwavelength extinction data is the lack of a unique solution (Liu *et al.* 1999). As we see from Fig. 12, several solutions are consistent with the 1995/HST data. To further constrain the solution, we may add constraints from other observations (other occultations, scattering versus phase angle, polarization versus phase angle). With the F ring we face an additional problem due to its known longitudinal and temporal inhomogeneity. The problems encountered in this analysis emphasize the need for simultaneous multiple wavelength observations of stellar occultations by planetary rings.

REFERENCES

Bohren, C. F., and D. R. Huffman 1983. *Absorption and Scattering of Light by Small Particles*. Wiley-Interscience, New York.

Borderies, N., P. Goldreich, and S. Tremaine 1983. The variations in eccentricity and apse precession rate of a narrow ring perturbed by a close satellite. *Icarus* **53**, 84–89.

Borderies, N., P. Goldreich, and S. Tremaine 1984. Excitation of inclinations in ring-satellite systems. *Astrophys. J.* **284**, 429–434.

Bosh, A. S. 1994. *Stellar Occultation Studies of Saturn's Rings with the Hubble Space Telescope*. Ph.D. thesis, Department of Earth, Atmospheric, and Planetary Sciences, Massachusetts Institute of Technology, Cambridge.

Bosh, A. S., and S. W. McDonald 1992. Stellar occultation candidates from the Guide Star Catalog. I. Saturn, 1991–1999. *Astron. J.* **103**, 983–990.

Bosh, A. S., and A. S. Rivkin 1996. Observations of Saturn's inner satellites during the May 1995 ring-plane crossing. *Science* **272**, 518–521.

Bosh, A. S., A. S. Rivkin, J. W. Percival, M. Taylor, and G. W. van Citters 1997. Saturn ring-plane crossing, May 1995: Pole precession and ring thickness. *Icarus* **129**, 555–561.

Burns, J. A., J. N. Cuzzi, and M. R. Showalter 1983. Discovery of gossamer rings. *Bull. Amer. Astron. Soc.* **15**, 1013–1014.

Clark, R. N. 1980. Ganymede, Europa, Callisto, and Saturn's rings: Compositional analysis from reflectance spectroscopy. *Icarus* **44**, 388–409.

Cuzzi, J. N. 1985. Rings of Uranus—Not so thick, not so black. *Icarus* **63**, 312–316.

Elliot, J. L., R. G. French, K. J. Meech, and J. H. Elias 1984. Structure of the uranian rings. I. Square-well model and particle-size constraints. *Astron. J.* **89**, 1587–1603.

Elliot, J. L., A. S. Bosh, M. L. Cooke, R. C. Bless, M. J. Nelson, J. W. Percival, M. J. Taylor, J. F. Dolan, E. L. Robinson, and G. W. van Citters 1993. An occultation by Saturn's rings on 1991 October 2–3 observed with the Hubble Space Telescope. *Astron. J.* **106**, 2544–2572.

Esposito, L. W., C. C. Harris, and K. E. Simmons 1987. Features in Saturn's rings. *Astrophys. J.* **63**, 749–770.

Estrada, P. R., and J. N. Cuzzi 1996. Voyager observations of the color of Saturn's rings. *Icarus* **122**, 251–272.

French, R. G., P. D. Nicholson, M. L. Cooke, J. L. Elliot, K. Matthews, O. Perkovic, E. Tollestrup, P. Harvey, N. J. Chanover, M. A. Clark, E. W. Dunham, W. Forrest, J. Harrington, J. Pipher, A. Barucci, A. Brahic, C. Ferrari, I. Grenier, F. Roques, B. Sicardy, and M. Arndt 1993. Geometry of the Saturn system from the 3 July 1989 occultation of 28 Sgr and Voyager observations. *Icarus* **103**, 163–214.

French, R. G., K. J. Hall, C. McGhee, P. D. Nicholson, J. Cuzzi, L. Dones, and J. Lissauer 1998. The peregrinations of Prometheus. *Bull. Am. Astron. Soc.* **30**, 1141.

Graps, A. L., A. L. Lane, L. J. Horn, and K. E. Simmons 1984. Evidence for material between Saturn's A and F rings from the Voyager 2 photopolarimeter experiment. *Icarus* **60**, 409–415.

Greenberg, R., D. R. Davis, W. K. Hartmann, and C. R. Chapman 1977. Size distribution of particles in planetary rings. *Icarus* **30**, 769–779.

Grundy, W. M., and B. Schmitt 1998. The temperature-dependent near-infrared absorption spectrum of hexagonal H_2O ice. *J. Geophys. Res.* **103**, 25,809–25,822.

Grundy, W. M., M. W. Buie, J. A. Stansberry, J. R. Spencer, and B. Schmitt 1999. Near-infrared spectra of icy outer Solar System surfaces: Remote determination of H_2O ice temperatures. *Icarus* **142**, 536–549.

Harrington, J., M. L. Cooke, W. J. Forrest, J. L. Pipher, E. W. Dunham, and J. L. Elliot 1993. IRTF observations of the occultation of 28 Sgr by Saturn. *Icarus* **103**, 235–252.

Hartmann, W. K. 1969. Terrestrial, lunar, and interplanetary rock fragmentation. *Icarus* **10**, 201–213.

Hubbard, W. B., C. C. Porco, D. M. Hunten, G. H. Rieke, M. J. Rieke, D. W. McCarthy, V. Haemmerle, R. Clark, E. P. Turtle, J. Haller, B. McLeod, L. A. Lebofsky, R. Marcialis, J. B. Holberg, R. Landau, L. Carrasco, J. Elias, M. W. Buie, S. E. Persson, T. Boroson, S. West, and D. J. Mink 1993. The occultation of 28 Sgr by Saturn: Saturn pole position and astrometry. *Icarus* **103**, 215–234.

Keyes, C. D. 1995. *Faint Object Spectrograph Instrument Handbook*. STScI, Baltimore.

Kolvoord, R. A., J. A. Burns, and M. R. Showalter 1990. Periodic features in Saturn's F ring: Evidence for nearby moonlets. *Nature* **345**, 695–697.

Kuiper, G. P., D. P. Cruikshank, and U. Fink 1970. The composition of Saturn's rings. *Sky & Telescope* **39**, 14.

Lane, A. L., C. W. Hord, R. A. West, L. W. Esposito, D. L. Coffeen, M. Sato, K. E. Simmons, R. B. Pomphrey, and R. B. Morris 1982. Photopolarimetry from Voyager 2: Preliminary results on Saturn, Titan, and the rings. *Science* **215**, 537–543.

Lebofsky, L. A., T. V. Johnson, and T. B. McCord 1970. Saturn's rings: Spectral reflectivity and compositional implications. *Icarus* **13**, 226–230.

Lissauer, J. J., and S. J. Peale 1986. The production of "braids" in Saturn's F ring. *Icarus* **67**, 358–374.

Liu, Y., W. P. Arnott, and J. Hallett 1999. Particle size distribution retrieval from multispectral optical depth: Influences of particle nonsphericity and refractive index. *J. Geophys. Res.* **104**, 31,753–31,762.

Marouf, E. A., G. L. Tyler, and P. A. Rosen 1986. Profiling Saturn's rings by radio occultation. *Icarus* **68**, 120–166.

McGhee, C. A., P. D. Nicholson, R. G. French, and K. J. Hall 2001. HST observations of Saturnian satellites during the 1995 ring plane crossings. *Icarus* **152**, 282–315.

Murray, C. D., and S. M. Giuliatti Winter 1996. Periodic collisions between the moon Prometheus and Saturn's F ring. *Nature* **380**, 139–141.

Murray, C. D., M. K. Gordon, and S. M. Giuliatti Winter 1997. Unraveling the strands of Saturn's F ring. *Icarus* **129**, 304–316.

Nicholson, P., M. L. Cooke, and E. Pelton 1990. An absolute radius scale for Saturn's rings. *Astron. J.* **100**, 1339–1362.

Nicholson, P. D., and C. Porco 1988. A new constraint on Saturn's zonal gravity harmonics from Voyager observations of an eccentric ringlet. *J. Geophys. Res.* **93**, 10,209–10,224.

Nicholson, P. D., D. P. Hamilton, K. Matthews, and C. F. Yoder 1992. New observations of Saturn's coorbital satellites. *Icarus* **100**, 464–484.

Nicholson, P. D., M. R. Showalter, L. Dones, R. G. French, S. M. Larson, J. J. Lissauer, C. A. McGhee, P. Seitzer, B. Sicardy, and G. E. Danielson 1996. Observations of Saturn's ring-plane crossings in August and November 1995. *Science* **272**, 509–515.

Nicholson, P. D., R. G. French, and A. S. Bosh 1999. The F ring: Saturn's crooked halo? *Bull. Am. Astron. Soc.* **31**, 1229.

Nicholson, P. D., R. G. French, E. Tollestrup, J. N. Cuzzi, J. Harrington, K. Matthews, O. Perkovic, and R. J. Stover 2000. Saturn's rings I: Optical depth profiles from the 28 Sgr occultation. *Icarus* **145**, 474–501.

Olkin, C. B., and A. S. Bosh 1996. The inclination of Saturn's F ring. *Bull. Am. Astron. Soc.* **28**, 1125.

Pilcher, C. B., C. Chapman, L. A. Lebofsky, and H. H. Kieffer 1970. Saturn's rings: Identification of water frost. *Science* **167**, 1372–1373.

Pollack, J. B., and J. N. Cuzzi 1980. Scattering by nonspherical particles of size comparable to a wavelength: A new semi-empirical theory and its application to tropospheric aerosols. *J. Atmos. Sci.* **37**, 868–881.

Roddier, F., C. Roddier, A. Brahic, C. Dumas, J. E. Graves, M. J. Northcott, and T. Owen 2000. Adaptive optics observations of Saturn's ring plane crossing in August 1995. *Icarus* **143**, 299–307.

Showalter, M. R. 1994. Tracking clumps in Saturn's F ring. *Bull. Am. Astron. Soc.* **26**, 1150–1151.

Showalter, M. R. 1996. The life-cycle of clumps in Saturn's F ring. *Bull. Am. Astron. Soc.* **28**, 1125.

Showalter, M. R. 1997. Dynamics of clumps in Saturn's F ring. *Bull. Am. Astron. Soc.* **29**, 999.

Showalter, M. R., and J. A. Burns 1982. A numerical study of Saturn's F-ring. *Icarus* **52**, 526–544.

Showalter, M. R., and P. D. Nicholson 1990. Saturn's rings through a microscope: Particle size constraints from the Voyager PPS scan. *Icarus* **87**, 285–306.

Showalter, M. R., J. B. Pollack, M. E. Ockert, L. R. Doyle, and J. B. Dalton 1992. A photometric study of Saturn's F ring. *Icarus* **100**, 394–411.

Showalter, M. R., J. A. Burns, and D. P. Hamilton 1998. Saturn's "Gossamer" ring: The F ring's inner sheet. *Bull. Am. Astron. Soc.* **30**, 1044.

Showalter, M. R., L. Dones, and J. J. Lissauer 1999. Interactions between Prometheus and the F ring. *Bull. Am. Astron. Soc.* **31**, 1228.

Shure, M., D. W. Toomey, J. T. Rayner, P. M. Onaka, and A. T. Denault 1994. NSFCAM: A new infrared array camera for the NASA Infrared Telescope Facility, presented at Instrumentation in Astronomy VIII Kona, HI, 25–33.

Synnott, S. P., R. J. Terrile, R. A. Jacobson, and B. A. Smith 1983. Orbits of Saturn's F ring and its shepherding satellites. *Icarus* **53**, 153–158.

Tyler, G. L., V. R. Eshleman, J. D. Anderson, G. S. Levy, G. F. Lindal, G. E. Wood, and T. A. Croft 1981. Radio science investigations of the Saturn system with Voyager I: Preliminary results. *Science* **212**, 201–206.

van de Hulst, H. C. 1981. *Light Scattering by Small Particles*. Dover, New York.

Warren, S. G. 1984. Optical constants of ice from the ultraviolet to the microwave. *Appl. Opt.* **25**, 1206–1225.

Zebker, H. A., E. A. Marouf, and G. L. Tyler 1985. Saturn's rings: Particle size distributions for thin layer models. *Icarus* **64**, 531–548.